

Experimental verification of an LiDAR based Gust Rejection System for a Quadrotor UAV

Arthur P. Mendez, James F. Whidborne, Lejun Chen

Abstract—This paper assesses the use of a ground-based wind measuring LiDAR (Light Detection and Ranging) for remote sensing of incoming wind gusts at the landing site of an autonomous quadrotor. The experimental verification results show that the scalar measurements from the LiDAR were able to recreate the horizontal wind vector even with wind direction variation. Comparisons were conducted against conventional cup anemometers with wind vanes, and these show a good correlation. Upwind LiDAR measurements were used to predict the downstream wind using a transport model. This prediction compared with the downwind measurement shows a good correlation. This wind preview information from the LiDAR is then incorporated into a disturbance feedforward control scheme to increase the gust resilience of the vehicle. Simulation and experimental results demonstrate the system's efficacy.

I. INTRODUCTION

A challenging task in the outdoor autonomous operations of quadrotors is to maintain baseline control performance in the presence of wind/gusts. As a transient and unknown disturbance input of the system, wind/gusts can cause significant deviations in the quadrotor motion during its most vulnerable stage in flight; its take-off and landing into a charging station.

Most research on quadrotor gust rejection control has modelled wind as an external disturbance and used model-based robust filters or observers to estimate the wind disturbance [2], e.g. Active Disturbance Rejection Control (ADRC) [15], [25], the Disturbance Observer (DOB) approach [5], [8]–[11], and the Kalman filtering methods [1], [3], [7]. These have mostly proved to be applicable but may suffer from estimation phase delay and convergence error due to model plant mismatch and the lack of systematic tuning methods. The computation load raised by onboard wind estimation is another limitation for smaller drones. Wind estimation can also be achieved by using onboard wind measurement devices [14], [24]. While these methods can measure the wind at the exact location of the drone or provide the preview wind information for control, the measurement values are contaminated through the influence of the drone propellers on the surrounding air. This could also induce some level of unmodeled aerodynamic effects. Moreover, the added instrumentation also incurs a weight penalty. Some other methods



Fig. 1. Autonomous quadrotor hovering above its ground/charging station

directly utilise the existing onboard sensor measurements and the Wind Estimation Triangle to calculate the wind vectors [6], [12], [13], but these methods are sensitive to the measurements errors.

LiDAR (Light Detection and Ranging) is a form of laser anemometry, which for wind measurement applications utilises the Doppler-shift in the frequency of back-scattered light to measure wind speed. LiDAR's remote sensing capability has been used to detect wind disturbances in the aerospace industry. For example, [23] used onboard LiDARs mounted on the nose of a fixed-wing aircraft to investigate the characterisation of wake vortices and improve the gust load alleviation performance. In [24], two tethered transceiver units (telescopes) of the LiDAR system mounted on a multi-rotor UAV gives separate line-of-sight measurements for wind vector reconstruction. Recently, [28], [29] developed an H_∞ inner-loop preview controller to aid the autonomous landing of highly flexible aircraft. The LiDAR was assumed to be mounted onboard and the simulation results show the efficacy of the method.

Ideally, a wind preview system for gust rejection control of autonomous quadrotors would be part of a ground-based infrastructure such as the ground/charging station shown in Fig. 1. Thus there would be no weight penalty. This paper investigates this approach by using a *ground*-based LiDAR system to remotely measure the incoming gusts at the landing site and so improve the gust rejection capability of the quadrotor. A line-of-sight (LOS) LiDAR unit is integrated with the ground station. A motorised mount is devised for

This work was supported by industrial sponsor Herotech8 www.herotech8.com

Arthur P. Mendez is a PhD student in the Dynamics Simulation and Control Group, Cranfield University, Cranfield MK43 0AL, United Kingdom. a.mendez@cranfield.ac.uk

James F. Whidborne is a Reader in the Centre for Aeronautics, Cranfield University. j.f.whidborne@cranfield.ac.uk

Lejun Chen is with the Department of Electronic and Electrical Engineering, University College London. lejun.chen@ucl.ac.uk

the LiDAR unit to allow scanning and hence horizontal wind reconstruction of the incoming gust. This scanning method makes the estimation tolerant to wind direction changes at the landing site. To verify the precision and accuracy of the proposed scanning method, a pair of anemometers are set up around the ground station. The wind preview information, obtained from the LiDAR is then incorporated into a disturbance feedforward controller for the quadrotor. This feedforward controller is designed based on an aerodynamic trim analysis of the quadrotor at varying wind speeds and it outputs attitude commands for the quadrotor's onboard attitude controller. In this system architecture, the feedforward controller is implemented at the ground station along with the LiDAR, and hence a modification of the onboard inner-loop attitude controller or the addition of extra hardware onto the vehicle is avoided.

The main contributions of this paper are the development and experimental verification of a wind preview system for a quadrotor using a miniaturised ground-based LiDAR system. The methods ensure that the line-of-sight LiDAR can capture both the amplitude and the direction of the wind. The accuracy of the procedure is verified via a comparison of the LiDAR system with conventional wind-cup anemometers and wind vanes. Flight tests were conducted to verify the correlation between quadrotor motion and LiDAR measurements. Finally, experimental data gathered from the ground-based mini-LiDAR system was applied to a nonlinear simulation model using aerodynamic coefficients obtained from the Weybridge wind tunnel at Cranfield University. These results demonstrate the efficacy of the gust rejection control law for a quadrotor UAV.

The remaining sections are structured as follows, Section II details the system architecture and introduces its various components. Section III summarizes the methodologies used for the wind preview estimation and gust rejection control. Section IV details the experiments and discusses both the nonlinear simulation and the experimental results. Finally, Section V provides concluding remarks and future work to be conducted.

II. THE SYSTEM ARCHITECTURE

The overall architecture of the gust rejection system for a quadrotor UAV is shown in Fig. 2. To reduce the input axis misalignment of the LiDAR's LOS measurements, the remote wind is estimated using a horizontal scanning procedure. The wind predictor component in Figure 2 reconstructs the wind vector from the LiDAR scanning and also utilises a wind propagation model to predict the wind at the current position of the quadrotor. The position of the quadrotor within the landing site is acquired using a vision based positioning system involving fiducial markers placed around the landing pad and the ArUco library developed for the camera-based navigation [22]. Note that in Fig. 2, the outer-loop control law combines the feedforward and the baseline guidance control outputs. These outputs are then used as the commands for the on-board attitude controller which then has the capability to compensate for the incoming wind. Here

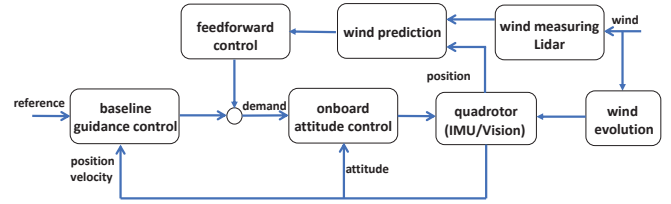


Fig. 2. Overall system architecture

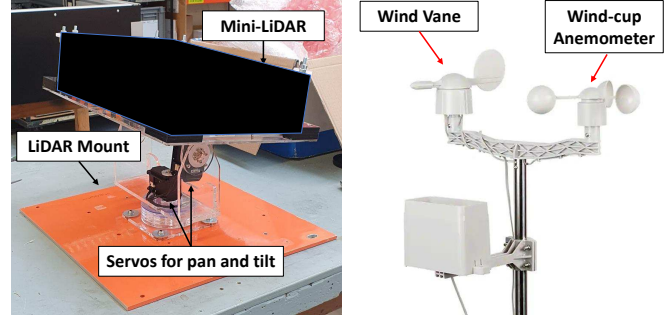


Fig. 3. LiDAR unit on its mount and the wind-cup anemometer with a wind vane

all the system components except for the onboard attitude controller are ground-based and are integrated with the ground station. The details of the wind measuring LiDAR, the horizontal scanning procedure, and the flight validation platform are described in the subsequent sections.

A. Wind Measuring Mini-LiDAR

The miniaturised LiDAR unit used in this research is a continuous wave (CW) coherent wind LiDAR system that utilises the infra-red band for measurement. The size of this prototype unit is 35cm × 25cm × 12cm and its weight is less than 5kg. It is a class 3b laser capable of measuring wind speed at a high sample rate with a measurable range that well exceeds the flight envelope of most multi-rotor UAVs. Detailed specification of the LiDAR unit is omitted here due to commercial sensitivity.

The LOS nature of the LiDAR measurements introduces the possibility of misalignment between the LiDAR beam direction and the actual wind direction [17], [27], [27]. A common solution to which is to use a scanning procedure to reconstruct the wind vector [17]. To carry out the LiDAR scanning in the landing site, a mechanised mount was used. The mount uses servo motors to pan and tilt the entire LiDAR unit. Since the quadrotor is in close proximity with the ground during its take-off and landing stage, it is assumed that the vertical component of the wind is negligible. Consequently, only the horizontal components of the wind require reconstruction for gust rejection; this greatly reduces the complexity of the scanning procedure which is further discussed in Section III-B.

To verify the precision and accuracy of the mini-LiDAR unit, standard off-the-shelf wind-cup anemometers with a wind vane (see Fig. 3) were used to determine the wind speed. The anemometers were calibrated in the open-circuit

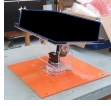

Hardware	Description
	<ul style="list-style-type: none"> • LiDAR motorised mount with pan and tilt capability • Two identical DYNAMIXEL MX-64AT motors used for each axis rotation • Pan/yaw range of 0 to 360 degrees • Tilt range 0 to +45 degrees • Scan rate constrained to 60 deg/s for pan due to mechanical limitations of mount.
	<ul style="list-style-type: none"> • Calibrated wind speed range 3m/s to 15m/s • No active electronics, uses magnets and magnetic reed switches to encode windspeed. • Raw data output rate varies, higher wind speed results in more switch closes, averaged to a 10Hz output. • Wind vane with 16 measurable positions, i.e. resolution of 22.5 degrees.

Fig. 4. Key hardware components of the wind sensing system.

Weybridge wind tunnel at Cranfield University for a wind-speed range of 3 to 15 ms^{-1} . More details on the key hardware components that make up the wind sensing system are shown in Fig. 4.

B. Quadrotor Flight-test Platform

An autonomous quadrotor platform was integrated with the wind sensing system to experimentally assess the gust rejection control. Flight tests were conducted with the quadrotor set to hover and hold a position above the ground station while the LiDAR and anemometers were measuring the wind around the test site. Fig. 5 shows the overall system architecture of the flight validation platform.

A DJI Mavic 2 quadrotor was used for the tests. The aircraft weighs approximately 900g with a maximum rated wind speed resistance of approximately 24 mph. The on-board sensor suite includes a vision-based system for obstacle avoidance and translation velocity estimation, GPS + GLONASS for positioning, a downward-facing ultrasonic sensor along with a barometer for height estimation, and dual IMUs and magnetometer for velocity and attitude estimation. The DJI Android software developer kit (SDK) was used to access the onboard sensor data and to send control commands to the onboard flight computer. The quadrotor position w.r.t. the ground station is acquired using the ArUco positioning system [22]. Its visual markers are placed on the landing pad inside the ground station. The main onboard camera feed is used for marker detection and localisation. This positioning node along with the DJI SDK flight controller was deployed as an Android application onto the DJI's smart controller as shown in Fig. 5.

The guidance controller outputs the attitude commands and is housed in the ground station computer. The attitude command outputs are the summation of the feedback controller and the disturbance feedforward controller. It should be noted here that only the outer-loop control of the quadrotor was taken off-board and housed in the ground station, the inner-loop onboard controller was not modified.

The guidance controller with disturbance feedforward control was developed in Simulink and deployed onto the hardware using Simulink's embedded coder. The ground station computer also houses the wind predictor subsystem which uses the upwind LOS measurements from the LiDAR to reconstruct the horizontal wind vector and utilises the

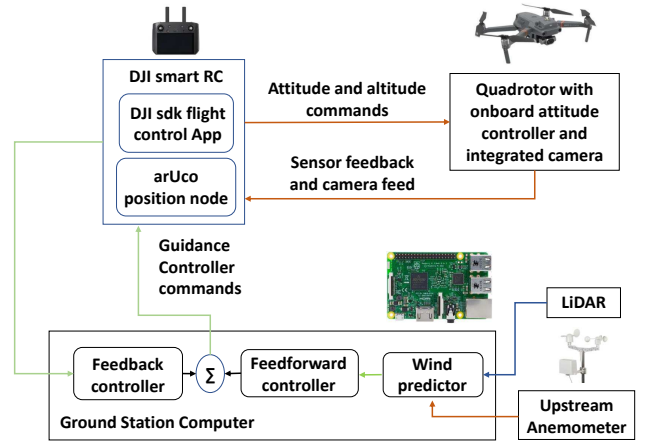


Fig. 5. Quadrotor flight-test platform architecture. Orange arrows indicate radio based communication, blue for serial connection, and green indicates communication through ROS.




Hardware	Description
	<ul style="list-style-type: none"> • DJI Mavic 2 Enterprise Dual. • Take-off weight 899 g and diagonal length 354 mm • Max wind resistance speed of 24 mph • Integrated on-board visual and thermal camera • DJI on-board flight computer with dual IMUs, magnetometer, ultrasonic, omnidirectional vision based obstacle sensing, and GPS + GLONASS. • Operating frequency 2.400 - 2.4835, 5.725 - 5.850 GHz
	<ul style="list-style-type: none"> • DJI smart controller with Wi-Fi for android application deployment • DJI sdk flight control programming for external source for outer-loop control of drone. • Processes camera-feed for ArUco marker detection and localisation • ROS node for receiving guidance control commands and sending DJI sensor and positioning data
	<ul style="list-style-type: none"> • Raspberry Pi 3+, quad Core 1.2GHz Broadcom BCM2837 64bit CPU, 1 GB RAM • Hosts the guidance controller with disturbance feedforward control • Hosts the wind predictor algorithm • ROS master node and hosts the ROS nodes for guidance controller and the wind sensors.

Fig. 6. key hardware components of the quadrotor flight-test platform

wind propagation model (detailed in section III-A) to provide a wind preview signal for the feedforward controller. Robot Operating System (ROS) www.ros.org is used as the communication protocol between the guidance controller, the smart RC, and the wind predictor nodes. The guidance controller outputs from the ground station are first sent to the smart RC application after which they are sent to the onboard flight controller through the radio link between the vehicle and the RC. The key hardware components used in the test platform apart from wind sensors are detailed in Fig. 6.

III. METHODOLOGIES

The wind propagation/prediction, LiDAR scanning, and gust rejection control methodologies are discussed in this section.

A. Wind Propagation Model

This subsection describes the transport model used to capture the wind propagation from the upstream to the

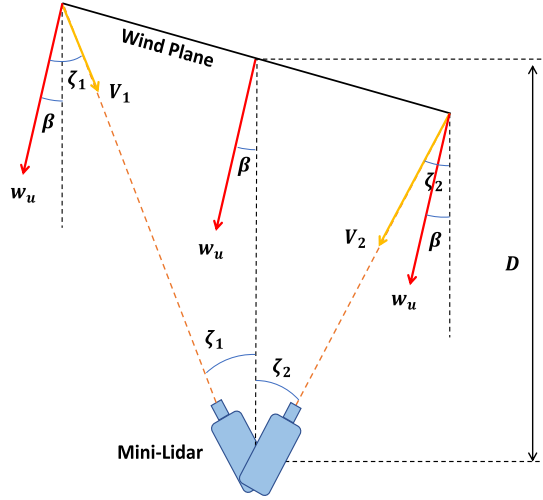


Fig. 7. LiDAR horizontal scan of the incoming wind plane

downstream location. The schematic is shown in Fig. 7. The transport model is defined as

$$w'_d(t) = w_u(t - \tau) \quad (1)$$

where $w'_d(t)$ represents the predicted downstream windspeed, $w_u(t)$ denotes the upstream wind measurement and τ is the wind transport delay between the upstream and the downstream wind planes given by

$$\tau = \frac{D \cos(\text{MA}(\beta))}{\text{MA}(w_u)} \quad (2)$$

where β denotes the wind direction in the reference frame of the LiDAR, $\text{MA}(\cdot)$ represents the moving average of the measurements, and the parameter D denotes the known distance between the upstream and downstream measurement points.

B. Lidar Scanning Procedure

The scanning procedure used to reconstruct the wind speed vector is outlined in this subsection. Because the vertical component of the wind vector is negligible during the take-off/landing process, only a horizontal wind vector needs to be reconstructed. Fig. 7 shows the schematic of the horizontal LiDAR scanning using two LOS measurements. The LiDAR measures the wind vectors at two different incidences, ζ_1 and ζ_2 , in the anti-clockwise and clockwise directions respectively.

From Fig. 7, the wind direction is expressed as:

$$\beta = \tan^{-1} \left(\frac{V_2 \cos \zeta_1 - V_1 \cos \zeta_2}{V_2 \sin \zeta_1 + V_1 \sin \zeta_2} \right) \quad (3)$$

where V_1 and V_2 are the two LOS measurements from the LiDAR during each scan cycle.

Let $|\zeta_1| = |\zeta_2| = \zeta$, then (3) is equivalent to

$$\beta = \tan^{-1} \left(\left(\frac{V_2 - V_1}{V_2 + V_1} \right) \cot \zeta \right) \quad (4)$$

Suppose β is obtained from (4), then the magnitude of the upstream horizontal wind vector is calculated as

$$|w_u| = \frac{V_1}{\cos(\beta + \zeta_1)} = \frac{V_2}{\cos(\zeta_2 - \beta)} \quad (5)$$

The upwind wind vector measurement in the LiDAR beam's reference frame is then obtained as:

$$[w_u]_l = [|w_u| \cos \beta \quad |w_u| \sin \beta] \quad (6)$$

Once are the wind direction and the upwind horizontal wind vector obtained from (4) and (5), the downstream prediction in the LiDAR's reference frame, $[w'_d]_l$, can be obtained using (1) and (2).

C. Disturbance Feedforward Control

This section discusses the proposed feedforward controller shown in Fig. 2. Once a prediction of the downstream wind is obtained, a suitable control input needs to be calculated to counter the disturbance on the quadrotor. The proposed approach is to determine the trim state attitude of the aircraft for the corresponding wind disturbance. The trim attitudes for a set of wind speeds are pre-computed and deployed as a look-up table in the feedforward controller. This reduces the real-time computational requirements. Of course, this comes with the assumption that the disturbance is steady-state when in reality it is time-varying. The approach, although sub-optimal, serves as a good starting point about which a derivative component can be heuristically tuned to counter the transient effects of the wind disturbance.

Before determining the necessary attitude commands, the predicted downstream wind vector is rotated into the quadrotor body axes by:

$$[w'_d]_b = \begin{bmatrix} \cos \psi_l & \sin \psi_l \\ -\sin \psi_l & \cos \psi_l \end{bmatrix} [w'_d]_l \quad (7)$$

where the yaw orientation of the quadrotor in the LiDAR's reference frame, ψ_l , is obtained from measurements from the LiDAR and vehicle magnetometers. Once the predicted wind disturbance is obtained in the body axis of the drone, the feedforward attitude commands, θ_f and ϕ_f , are computed as follows:

$$\begin{aligned} \theta_f &= K_p \hat{\theta} + K_d \frac{d([w'_d]_{bx})}{dt} \\ \phi_f &= K_p \hat{\phi} + K_d \frac{d([w'_d]_{by})}{dt} \end{aligned} \quad (8)$$

where K_p and K_d denote the proportional and derivative gains of the feedforward controller. These were determined heuristically through simulations of a quadrotor model that accounts for the aerodynamics of the propellers in the presence of wind [21]. Here $\hat{\theta}$ and $\hat{\phi}$ denote the trim state pitch and roll angles of the quadrotor for the specified wind speed in its respective axes. The trim states are referenced as a precomputed look-up-table (LUT) obtained through an aerodynamic trim analysis of the quadrotor model in varying wind speeds:

$$[\hat{\theta} \quad \hat{\phi}] = \text{LUT}([w'_d]_b) \quad (9)$$

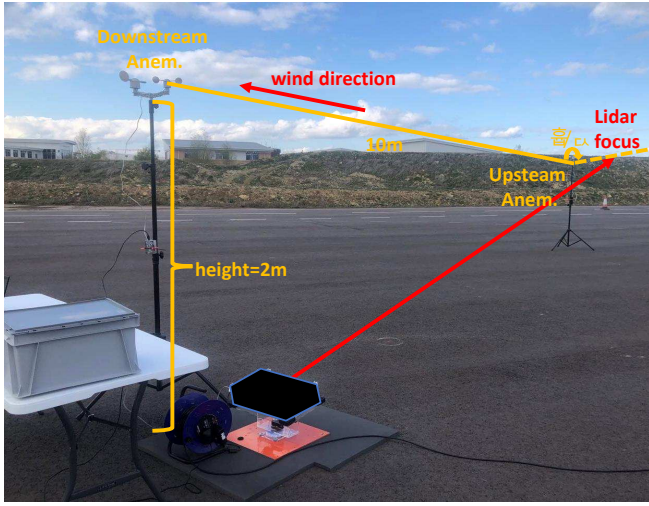


Fig. 8. LiDAR and anemometer experimental layout

The feedforward controller outputs are then cascaded with a conventional PID-based feedback controller that provides stability and robustness.

IV. RESULTS

In this section, the accuracy of the LiDAR, its scanning procedure, and the wind prediction methodology are verified using the upstream and downstream anemometers. Results of flight tests conducted using the quadrotor flight-test platform and the LiDAR are discussed. Finally, non-linear simulations conducted with the data from the LiDAR are presented.

A. LiDAR Accuracy Verification

The accuracy of LiDAR's LOS wind measurements is verified using the upstream anemometer. The experimental setup is shown in Fig. 8 where two anemometers are mounted on tripods 2m high and placed 10m apart along the approximate wind direction. As shown in Fig. 8, the LiDAR was placed next to the downwind anemometer. The mount for the LiDAR is inclined upwards to measure the wind speed next to the upstream anemometer. Notice that the location of the laser focus with respect to the LiDAR resolved in the inertial frame is perpendicular to the upwind anemometer wind plane.

The verification results are shown in Figs. 9 and 10. Fig. 9(a) compares the LiDAR wind measurements with the upstream anemometer. The LiDAR measurements bandwidth is higher, this implies that LiDAR has a better ability to capture gusts.

The cross-correlation analysis in Fig. 9(b) shows a maximum correlation of 0.9907 which is reached when the LiDAR measurement is back-shifted by 0.52sec, i.e. the LiDAR leads the upstream anemometer measurements by half a second. This is due to the inertia of the wind-cup anemometer. Because the LiDAR measurements are LOS and no scanning is employed in this test, the misalignment between the wind direction and the LiDAR's beam axis reduces the LiDAR's measurement accuracy.

Fig. 10(a) shows moving averages of the wind vane measurements about the LiDAR beam's axial direction (blue curve) along with the difference between the LiDAR and the upwind anemometer measurements (red curve). The peaks of the red curve are correlated to those of the blue curve signifying that the LiDAR LOS measurements can be corrected by considering the wind direction variation. The cosine of the wind vane measurements was used to correct the LiDAR LOS measurements, the results of which are shown in Fig. 10(b) along with the upstream anemometer measurements. Notice that in Fig. 10(b), the raw data from the LiDAR were processed using a window size of 1 minute.

B. Scanning Procedure Verification

During the tests, the LiDAR mount scanned horizontally in the general direction of the wind, i.e. according to the generic wind direction observed for the day of the test. This allows the sampling of multiple LOS measurements at different angles against the wind thus enabling the estimation of wind direction in the horizontal plane.

Fig. 11(a) shows the results of the estimation routine compared with the wind vane measurements. It can be seen that the wind direction estimated from the scan agrees well with the wind vane measurements but lags behind them slightly. This is primarily due to the time period of the scan itself, which was limited to 3 seconds because of mechanical constraints of the mount. The wind direction estimated from the scan process can be used to correct/reconstruct the horizontal wind vector. Fig. 11(b) compares the upwind anemometer measurements with the LOS measurements corrected using the wind direction estimates from the scan and those corrected using the wind vane measurements. Clearly, the LOS measurements corrected by the scanning routine are capable of tracking those corrected by the wind vane for the majority of the test duration.

C. Wind Propagation Model Verification

To verify the accuracy of the wind propagation model, both the upwind anemometer and LiDAR measurements were used to predict the wind speed at the downstream location according to (1). A comparison is shown in Fig. 12(a). Note that the horizontal wind vector reconstructed from the LiDAR measurements was used for the prediction. Both the upwind anemometer and LiDAR with wind vector reconstruction are capable of predicting the wind speed at the downwind location using the wind propagation model detailed in section III-A. Fig. 12(b) shows the cross-correlation analysis of both predictions against the downstream measurement. Both predictions are highly correlated; the LiDAR-based prediction leads the downwind measurement by approximately 0.5 s again due to the inertia of the anemometer.

Fig. 12(a) also shows the ability of the wind prediction to track the relatively small changes in wind speed magnitude at the downwind location very accurately. The main error between the predictions and the downwind measurement is the difference in magnitudes at the peaks and valleys of the wind speed variation. The temporal accuracy of the

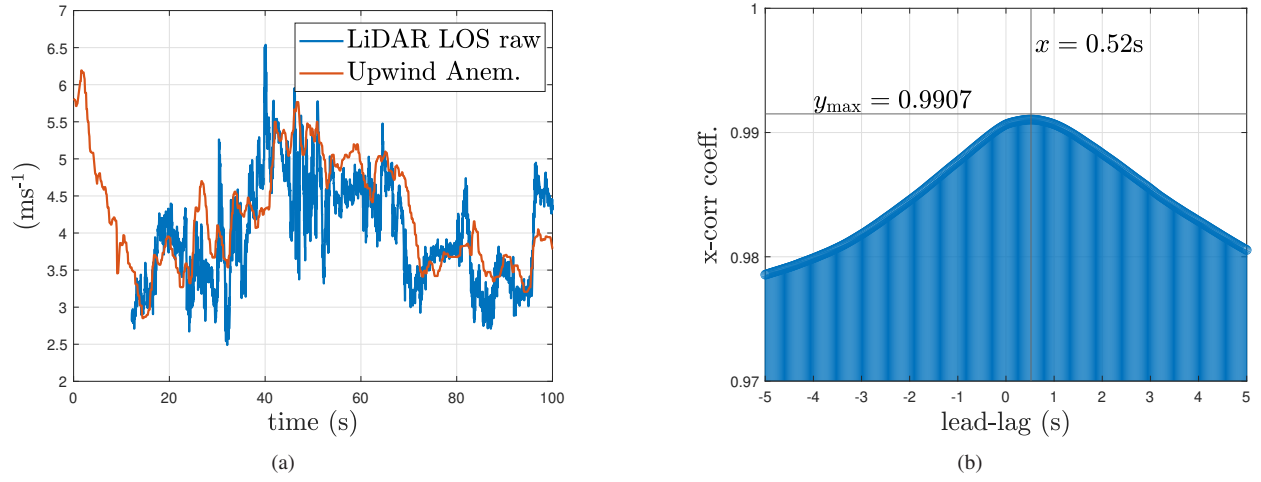


Fig. 9. (a) LiDAR and upwind anemometer measurements; (b) the cross correlation analysis; measurements

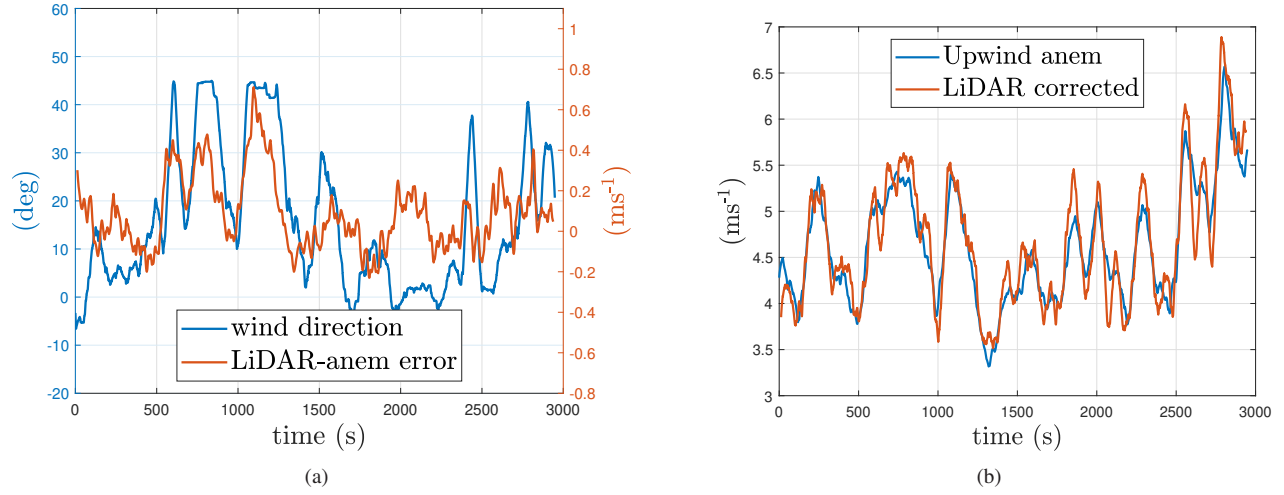


Fig. 10. (a) LiDAR-Anem. error against wind direction from wind vane (1min moving average); (b) LiDAR's LOS corrected using wind vane and anemometer measurements

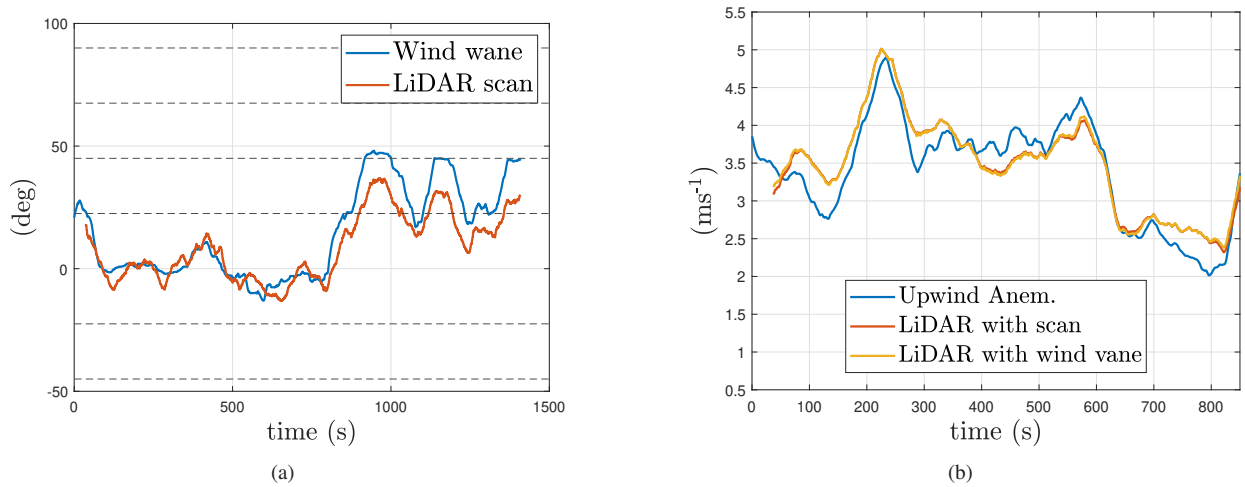


Fig. 11. (a) the wind direction estimates (LiDAR Vs wind vane); (b) true upwind anemometer measurements Vs the corrected wind speed LOS measurements

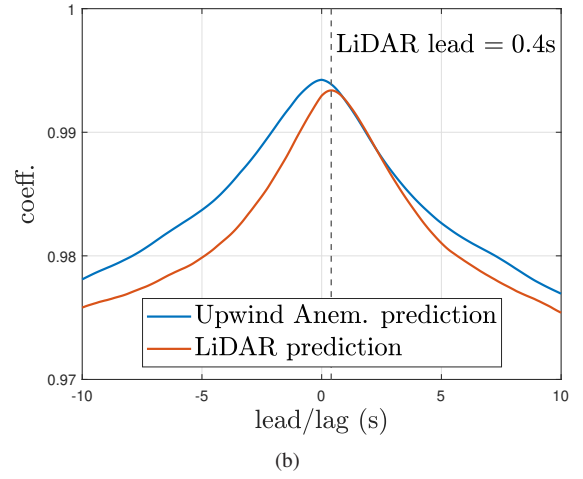
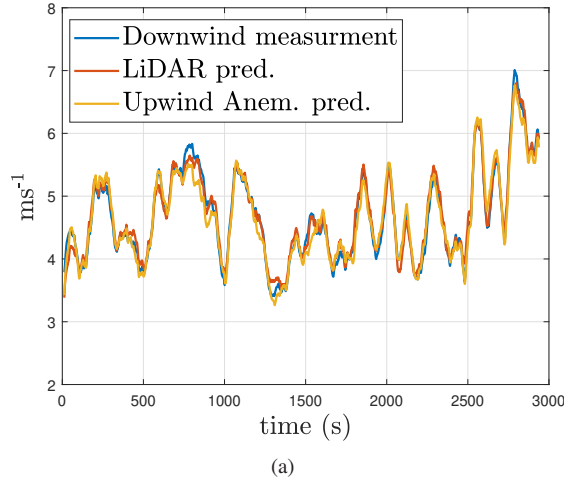


Fig. 12. (a) the true downwind anemometer measurements Vs the wind predictions at the downwind location; (b) the correlation between two wind predictions

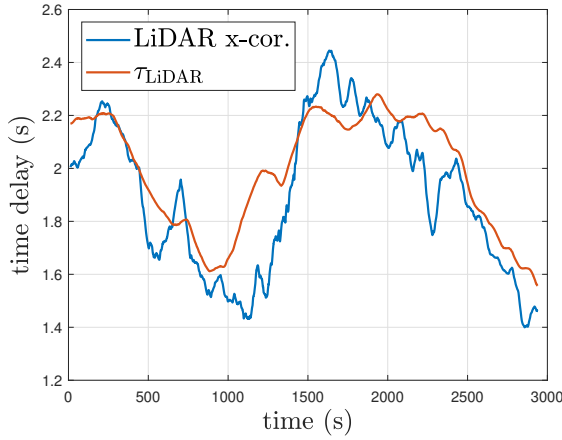


Fig. 13. transport delay from a moving window cross correlation analysis between upwind and downwind measurements Vs transport delay in wind propagation model during run-time

predictions is further verified in Fig. 13. Here the time delay from a moving window cross correlation analysis between the actual upwind LiDAR and downwind measurement is plotted against the transport delay calculated during the run-time of the wind propagation model. It should be noted here that the red curve in Fig. 13 is obtained using just the upwind measurements and the wind propagation model while the blue curve is generated by comparing both upwind and downwind measurements. The correlation between both signifies the ability of the wind propagation model to accurately estimate the transport delay between both measurement locations using just the upwind measurements.

D. Quadrotor Flight-test with LiDAR

The purpose of this flight test was an initial assessment of the position response of the quadrotor in wind and to observe correlations with the anemometer measurements and LiDAR preview; the feedforward controller was not implemented in the flight test. The main components of the flight test system are shown in Fig. 5. The DJI Mavic 2 was set to

hover and hold position above the ground station. A guidance controller using the visual ArUco markers for positioning was implemented in the ground station electronics. The downwind anemometer and LiDAR was set up next to the quadrotor to measure both the wind next to the quadrotor and the incoming wind respectively. Fig. 14 shows the quadrotor forward and lateral position tracking errors (blue curve) along with the anemometer and LiDAR measurements resolved to the corresponding axes (red curves). Clearly, the peaks in position tracking errors correspond to the transient regions (gusts) of the wind speed measurement. This is expected as the feedback controller drives the errors to zero when transients have died down.

Fig. 15 plots the wind acceleration obtained through numerical differentiation of the anemometer measurements and LiDAR preview data against a moving average of the quadrotor position error. Here a clear correlation is observed between the wind acceleration peaks and the position error with the wind acceleration signals having a slight lead. Moreover, the correlation becomes even more apparent and synced in time when the LiDAR's preview acceleration is passed through a low-pass Butterworth filter. This demonstrates the suitability of the wind acceleration to be used as a contributor in the disturbance rejection controller, realised through the feedforward controller derivative term detailed in Sec. III-C.

E. Quadrotor Gust Simulations

Gust simulations were conducted using a nonlinear quadrotor model containing detailed aerodynamic coefficients obtained from experiments conducted at the Weybridge wind tunnel in Cranfield University [20], [21]. Downwind anemometer time-series data recorded from the field tests was used as the wind disturbance signal sent into the quadrotor model while the LiDAR measurements were corrected using the scan procedure and used in conjunction with the wind propagation model to provide the wind preview signal for the feedforward controller. A snippet of the simulation result is shown in Fig. 16(d). The yellow curve is

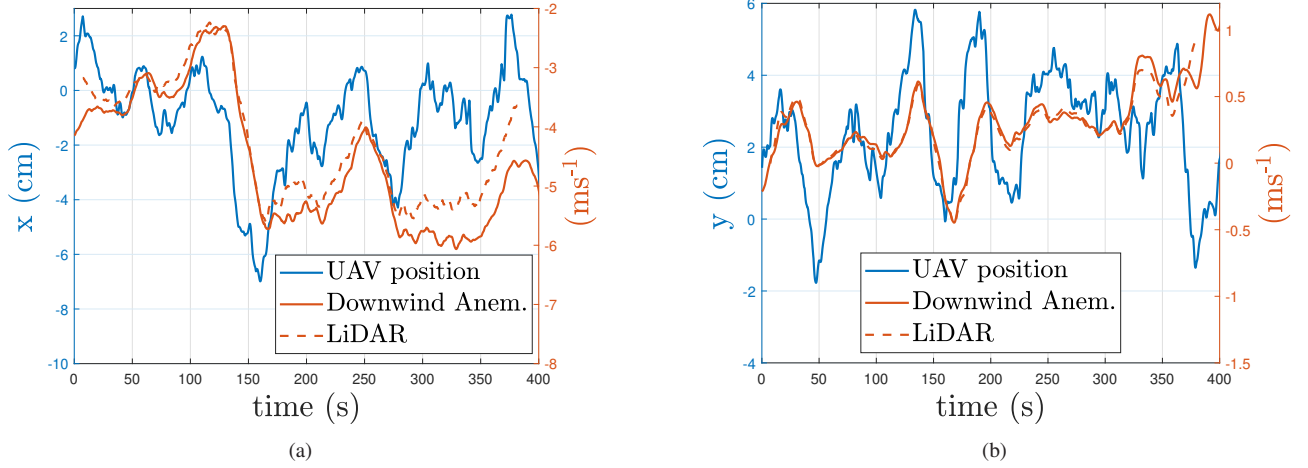


Fig. 14. (a) forward and (b) lateral position response comparison with downstream wind speed measurements from anemometer and predictions from LiDAR

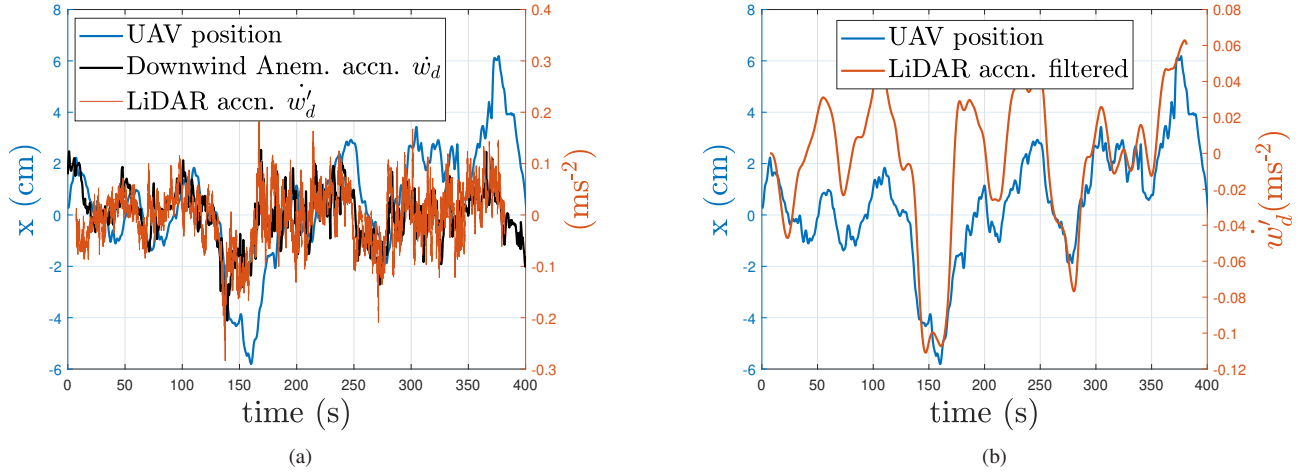


Fig. 15. (a) forward position response compared against wind acceleration obtained from downwind anemometer and LiDAR preview resolved to corresponding axis; (b) uses a low pass filter for the LiDAR's wind acceleration data

the wind predictor output which reconstructs the horizontal wind from the LOS measurements of the LiDAR (red curve) and passes it through the wind propagation model to predict the downstream wind speed. The blue curve denotes the actual measurement in the downstream location that is used as the disturbance input into the quadrotor model. Notice how the correction of the LOS measurements allows the wind preview to better capture the magnitude of the wind speed at the downstream location while the wind propagation model corrects for the time lead.

To assess the benefits of the proposed control law, two simulation scenarios were run. The first included the disturbance feedforward controller and the second had just the feedback controller. In both scenarios, the set-point for the quadrotor's position was a constant location and altitude. The high-frequency component of the upwind measurements was removed through a suitable Butterworth filter. Figures 16(a) and 16(b) compare the longitudinal and lateral tracking errors respectively. The altitude errors were similar for both

scenarios since the feedforward controller only compensates for the horizontal wind disturbances. The improvement in position holding performance of the quadrotor with feedforward control is more clearly shown in Fig. 16(c), where histograms of the longitudinal position tracking errors are shown. The lateral errors are omitted here for brevity due to their similarity with the longitudinal. These show that both the mean and the standard deviation are significantly improved, which implies that the accuracy and the precision of the position holding are improved with the wind preview from the LiDAR. Detailed values of the RMS and the standard deviation of the position tracking errors are listed in Table I.

The robustness of the feedforward controller was tested through Monte Carlo simulations involving various amounts of parameter uncertainties and transport delays acting inside the feedforward channel. The root-mean-square (RMS) of the horizontal position error is chosen as the performance metric. Multiplicative parameter uncertainty was introduced

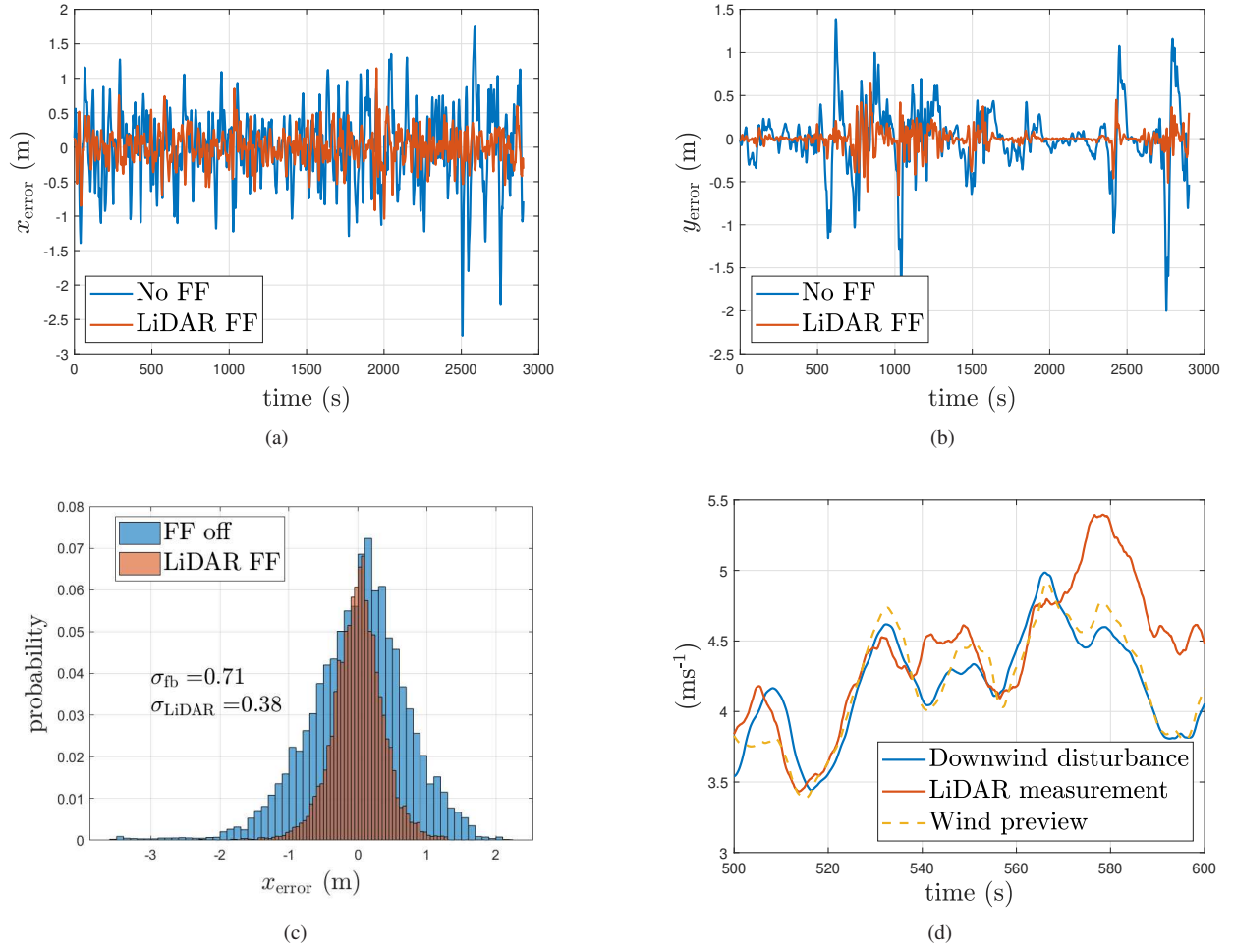


Fig. 16. (a) Errors in forward and (b) lateral position of the UAV (c) Histograms of the forward position tracking error with and without disturbance feedforward control (d) Wind signals used in simulation, downwind measurement (blue), the LiDAR's measurement (red) and its preview (yellow) for the feedforward controller.

TABLE I

POSITION HOLDING PERFORMANCE WITH AND WITHOUT DISTURBANCE FEEDFORWARD CONTROL

	RMS error	reduction	error σ	reduction
Baseline No FF	0.6980m	-	0.71	-
Anemometer FF	0.3964m	43.20%	0.4	43.70%
LiDAR FF	0.3742m	46.40%	0.38	46.50%

in the trim state attitudes used by the feedforward controller (detailed in Sec. III-C), the results of which are shown in Table II. Table III shows the results for the simulations with time delay introduced into the wind preview signal. The performance comparison in both these tables is against the baseline scenario without the feedforward control. It is clear that the gust rejection control law still improves the position tracking performance despite having parameter uncertainty in the trim state attitudes up to $\approx 90\%$ or a time delay of up to ≈ 2 s in the wind prediction.

V. CONCLUSION

Experiments were conducted to assess the feasibility of a ground-based LiDAR gust rejection control system for

TABLE II

PERFORMANCE COMPARISON WITH MULTIPLICATIVE UNCERTAINTY IN FEEDFORWARD CHANNEL

Uncertainty (%)	RMS error (m)	Performance. diff. (%)
10	0.14	+86.6
20	0.25	+76.97
30	0.29	+73.26
40	0.46	+57.90
50	0.51	+53.07
60	0.70	+35.41
70	0.75	+30.20
80	0.98	+9.34
90	0.93	+13.94
100	1.30	-20.15
110	1.36	-25.54
120	1.38	-27.42

quadrotor UAVs. The accuracy of the LiDAR wind speed measurements and the wind propagation model were verified using conventional wind-cup anemometers. Experimental results show that the LiDAR can measure transient and gusting of the wind more precisely than conventional anemometers. A horizontal wind scanning procedure is proposed to reduce

TABLE III

PERFORMANCE COMPARISON WITH TIME DELAY INTRODUCED IN
FEEDFORWARD CHANNEL

Time delay (s)	RMS error (m)	Performance. diff. (%)
0	0.12	+89.34
0.2	0.20	+81.42
0.4	0.27	+75.34
0.7	0.38	+64.46
0.9	0.48	+55.90
1	0.54	+50.10
1.2	0.74	+31.41
1.4	0.89	+17.67
1.8	0.95	+12.23
1.9	0.95	+12.07
2.2	1.25	-15.78

the effect of the axis-misalignment in the LiDAR's LOS measurements. Flight tests with the LiDAR system show a good correlation of the position response of the UAV with the LiDAR measurements. Finally, gust simulations of the UAV with experimental windspeed data demonstrate the potential efficacy of the proposed system. Comparisons against existing gust rejection methods and the flight-test of the feedforward controller remain to be performed; following which, investigations on utilizing this method for other UAV applications such as landings on fast-moving ground vehicles and sea vessels should be conducted.

ACKNOWLEDGMENT

This research was supported by Cranfield University and industrial sponsor Herotech8. We are thankful to our colleagues, Robin Gojon and Edward Anastassacos, Ciaran McMaster, and Adam Seward for their help with the design and development of the LiDAR mount and their support with the conduct of the experiments.

REFERENCES

- [1] V. Ayala-Alfaro, F. Torres-Del Carmen and J. Ramirez-Paredes, "Wind field estimation by small UAVs for rapid response to contaminant leaks," *International Conference on Unmanned Aircraft Systems*, pp. 1546–1552, 2020.
- [2] J. González-Rocha, C.A. Woolsey, C. Sultan, and S. F. J. De Wekker, "Sensing wind from quadrotor motion," *Journal of Guidance, Control, and Dynamics*, vol. 42, pp. 836–852, 2019.
- [3] J. Gonzalez-Rocha, C.A. Woolsey, C. Sultan, S. De Wekker and N. Rose, "Measuring atmospheric winds from quadrotor motion," *AIAA Atmospheric Flight Mechanics Conference*, pp. 1189, 2017.
- [4] X. Xiang, Z. Wang, Z. Mo, G. Chen, K. Pham, K and E. Blasch, "Wind field estimation through autonomous quadcopter avionics," *IEEE/AIAA Digital Avionics Systems Conference*, pp. 1–6, 2016.
- [5] D. Shi, Z. Wu and W. Chou, "Generalized extended state observer based high precision attitude control of quadrotor vehicles subject to wind disturbance," *IEEE Access*, vol. 6, pp. 32349–32359, 2018.
- [6] Y. Qu, Z. Xing and Y. Zhang, "Wind estimation using the position information from a hovering quadrotor," *IEEE Chinese Guidance, Navigation and Control Conference*, pp. 1345–1350, 2016.
- [7] Z. Xing, Y. Zhang, C. -Y. Su, Y. Qu and Z. Yu, "Kalman filter-based wind estimation for forest fire monitoring with a quadrotor UAV," *IEEE Conference on Control Technology and Applications*, pp. 783–788, 2019.
- [8] A. Aboudonia, A. El-Badawy and R. Rashad, "Active anti-disturbance control of a quadrotor unmanned aerial vehicle using the command-filtering backstepping approach," *Nonlinear Dynamics*, Vol. 90, pp. 581–597, 2017.
- [9] B. Xiao and S. Yin, "A new disturbance attenuation control scheme for quadrotor unmanned aerial vehicles," *IEEE Transactions on Industrial Informatics*, Vol. 13, pp. 2922–2932, 2017.
- [10] S. I. Azid, K. Kumar, M. Cirrincione and A. Fagioli, "Wind gust estimation for precise quasi-hovering control of quadrotor aircraft," *Control Engineering Practice*, Vol. 116, 2021.
- [11] G. Perozzi, D. Efimov, J. Biannic, L. Planckaert and P. Coton, "Wind estimation algorithm for quadrotors using detailed aerodynamic coefficients," *American Control Conference*, 2018.
- [12] P. P. Neumann, S. Asadi, A. J. Lilienthal, M. Bartholmai and J. H. Schiller, "Autonomous gas-sensitive microdrone: wind vector estimation and gas distribution mapping," *IEEE Robotics & Automation Magazine*, vol. 19, pp. 50–61, 2012.
- [13] P. P. Neumann, and M. Bartholmai, "Real-time wind estimation on a micro unmanned aerial vehicle using its inertial measurement unit," *Sensors and Actuators A: Physical*, Vol. 235, pp. 300–310, 2015.
- [14] A. Paris, A. Tagliabue and J. P. How "Autonomous MAV landing on a moving platform with estimation of unknown turbulent wind conditions," *AIAA Scitech 2021 Forum*, pp. 378, 2021.
- [15] H. Yang, L. Cheng, Y. Xia and Y. Yuan, "Active disturbance rejection attitude control for a dual closed-loop quadrotor under gust wind," *IEEE Transactions on Control Systems Technology*, vol. 26, pp. 1400–1405, 2017.
- [16] F. Dunne, L. Pao, A. Wright, B. Jonkman, N. Kelley and E. Simley, "Adding feedforward blade pitch control for load mitigation in wind turbines: Non-causal series expansion, preview control, and optimized FIR filter methods," *AIAA aerospace sciences meeting including the new horizons forum and aerospace exposition*, pp. 819, 2011.
- [17] D. Schlipf, L.Y. Pao and P.W. Cheng, "Comparison of feedforward and model predictive control of wind turbines using LiDAR," *IEEE Conference on Decision and Control*, pp. 3050–3055, 2012.
- [18] E. Simley, L. Pao, N. Kelley, B. Jonkman and R. Frehlich "LiDAR wind speed measurements of evolving wind fields," *AIAA Aerospace Sciences Meeting including the New Horizons Forum and Aerospace Exposition*, pp. 656, 2012.
- [19] C.B. Hasager, A. Peña, M.B. Christiansen, P. Astrup, M. Nielsen, F. Monaldo, D. Thompson and P. Nielsen, "Remote sensing observation used in offshore wind energy," *IEEE Journal of Selected Topics in Applied Earth Observations and Remote Sensing*, vol. 1, pp. 67–79, 2008.
- [20] V. Martinez, "Modelling of the flight dynamics of a quadrotor helicopter," *MSc Thesis, Cranfield University*, 2007.
- [21] A. Mendez, "A study into the effects of rotor tilt on the gust rejection properties of a quadrotor," *MSc Thesis, Cranfield University*, 2019.
- [22] S. Garrido-Jurado, R. Muñoz-Salinas, F.J. Madrid-Cuevas and M.J. Marín-Jiménez, "Automatic generation and detection of highly reliable fiducial markers under occlusion," *Pattern Recognition*, vol. 47, pp. 2280–2292, 2014.
- [23] N. Fezans, J. Schwithal and D. Fischenberg, "In-flight remote sensing and identification of gusts, turbulence, and wake vortices using a Doppler LiDAR," *CEAS Aeronautical Journal*, vol. 8, pp. 313–333, 2017.
- [24] N. Vasiljević, M. Harris, A.T. Pedersen, G.R. Thorsen, M. Pitter, J. Harris, K. Bajpai and M. Courtney, "Wind sensing with drone-mounted wind lidars: proof of concept," *Atmospheric Measurement Techniques*, vol. 13, pp. 521–536, 2020.
- [25] J. Han, "From PID to active disturbance rejection control," *IEEE Transactions on Industrial Electronics*, vol. 56, pp. 900–906, 2009.
- [26] X. Lyu, J. Zhou, H. Gu, Z. Li, S. Shen and F. Zhang, "Disturbance observer based hovering control of quadrotor tail-sitter VTOL UAVs Using H_∞ synthesis," *IEEE Robotics and Automation Letters*, vol. 3, pp. 2910–2917, 2018.
- [27] P. Towers, P and B. Jones, "Real-time wind field reconstruction from LiDAR measurements using a dynamic wind model and state estimation," *Wind Energy*, vol. 19, pp. 133–150, 2016.
- [28] Qi, P and Zhao, X and Palacios, R, "Autonomous landing control of highly flexible aircraft based on lidar preview in the presence of wind turbulence," *IEEE Transactions on Aerospace and Electronic Systems*, vol. 55, pp. 2543–2555, 2019.
- [29] H. Fournier, P. Massioni, M. Tu Pham, L. Bako, R. Vernay, and M. Colombo, "Robust gust load alleviation of flexible aircraft equipped with Lidar," *Journal of Guidance, Control, and Dynamics*, vol. 45, pp. 58–72, 2022.